Applied Catalysis A, General 643 (2022) 118804

Contents lists available at ScienceDirect

Applied Catalysis A, General

journal homepage: www.elsevier.com/locate/apcata

Tuning the co-catalyst loading for the optimization of thermo-photocatalytic hydrogen production over Cu/TiO_2

F. Platero, A. Caballero, G. Colón *

Instituto de Ciencia de Materiales de Sevilla, Centro Mixto Universidad de Sevilla-CSIC, Américo Vespucio s/n., 41092 Sevilla, Spain

ARTICLE INFO

Keywords:
Thermo-photocatalysis
Gas-phase
Hydrogen
Cu-TiO_2.
Water-gas-shift

ABSTRACT

We have optimized the H_2 production by methanol thermo-photocatalytic reforming in the gas phase using Cu/TiO_2 catalyst by tuning metal loading. Metal co-catalyst has been deposited by means of chemical reduction deposition. We have stated that thermo- and thermo-photocatalytic process leads to a notable H_2 production at 200 °C. By in-situ FTIR studies we evidenced that formate formation follows a different evolution depending on the reforming experiment. These surface formate would lead to CO formation through dehydration reaction. At higher Cu content the low CO selectivity denote that water-gas-shift reaction would predominate and exalt H_2 yield. Thus, different optimum Cu content is found for each reforming experiment. While for the photocatalytic reforming Cu/TiO_2 (2 wt%) is the best catalyst of the series, we should increase the Cu content to Cu/TiO_2 (5 wt %) to achieve the optimum performance for thermo-photocatalytic reforming of methanol.

1. Introduction

It is widely accepted that hydrogen, a clean and sustainable energy vector, is considered the ideal alternative of fossil fuels. Within the actual framework of the socioeconomical and environmental situation, green hydrogen will play a crucial role for a clean energy transition process [1]. Since many years, photocatalytic water splitting towards hydrogen evolution has attracted numerous attentions because of its green sustainability [2,3]. In spite of the huge efforts to generate hydrogen via powder-based solar water-splitting systems to date have unfortunately fallen short of the efficiency values required for large scale plants [4,5]. The challenge is to develop stable and efficient catalysts that can harvest solar light, using co-catalyst alternative to precious materials that would allow the scale-up and practical applications [6,7]. In this sense, promising studies at pilot plant scale have been recently reported [8–11].

Within this frame, green H_2 production from alcohol photocatalytic reforming reaction appears as a hot topic in the field of photocatalysis [12,13]. From the enormous literature on this field, TiO_2 based systems have provided the best performances [14]. However, some factors such as rapid recombination, the occurrence of backward reaction or even the deactivation by the formed intermediates hindered the development of H_2 production at large scale [15]. The use of metal co-catalysts, used as charge trapping sites, have demonstrated necessary in order to enhance the efficiency of the photocatalytic reaction by avoiding the electron–hole recombination processes [16–18]. It has been found that the addition of these noble metals could have different effects on the photocatalytic activity which is also strongly affected not only by the nature of metal but also by other parameters from sample history and metal features [19]. Alternatively to noble metals, copper-based catalysts have been extensively considered as a cheaper option [13,20–23].

In addition to this traditional strategy, the combination of heat and light has been recently suggested as a novel approach pursuing the improving efficiency of the photocatalytic process [24–26]. Thus, by the combination of classical thermo- and photo-catalytic processes, interesting synergistic effects have been reported that drastically enhances the hydrogen production through photoreforming reaction [25].

Due to the mechanistic complexity of this multicatalytic approach, which would involve different simultaneous reactions, the origin of this cooperative effect is still unclear. In principle, the synergistic improvement would be conditioned by the primary importance of single thermo- and photo- contributions on the kinetic behavior and reaction mechanism [27,28].

Moreover, most of the reported results do not cover the influence of the co-catalyst loading on such complex mechanism and the catalytic performance [27,28]. In the present paper we present an interesting study on methanol reforming through a multicatalytic approach, by combining heating and photonic excitation. For this scope, we use a

* corresponding author.
E-mail address: gcolon@icmse.csic.es (G. Colón).

https://doi.org/10.1016/j.apcata.2022.118804
Received 14 June 2022; Received in revised form 26 July 2022; Accepted 27 July 2022
Available online 30 July 2022

Cu/TiO_2 system with different Cu loading that could serve to explore how the mechanism is influenced by metal content and therefore condition the overall reaction performance.

2. Experimental

2.1. Catalysts preparation and characterisation

TiO_2 (Evonik P90) was used as photoactive support (Table 1 in Supporting Information). TiO_2 Evonik P90 exhibits higher surface area than widely used Evonik P25. Since the aim of this study is to see the effect of the amount of Cu loading on the catalytic activity, we decided to use this high surface area anatase to avoid the effect of metal agglomeration at increasing contents. Metal loading was performed through chemical reduction deposition procedure using copper nitrate as metal source. In this case, 0.5 g of support was suspended in 100 mL of water containing the stoichiometric amount of Cu precursor for a nominal loading between 1.0 and 5.0 wt%. Chemical reduction of metal precursor was achieved by using $NaBH_4$ as reducing agent. After adding the reducing agent at certain excess (1:20 molar ratio with respect to Cu), the suspension was stirred at room temperature for 30 min. The effectiveness of the deposition was always checked by adding more $NaBH_4$ to the filtrated liquid. We did not appreciate in any case any turbidity or color changes due to the presence of Cu. The obtained systems were filtered, thoroughly washed with distilled water and finally dried at 90 ºC. As prepared catalysts were labeled as Cu*n*P90, being *n* the nominal metal loading.

BET surface area measurements were carried out by N_2 adsorption using a Micromeritics 2000 instrument.

X-ray diffraction (XRD) patterns were obtained using a Siemens D-501 diffractometer with Ni filter and graphite monochromator, using the Cu Kα radiation as X-ray source., We have calculated the anatase fraction as well the mean crystallite size by Rietveld fitting using HighScore-Plus software, using the line broadening of corresponding diffraction peaks.

Diffuse reflectance UV–vis spectroscopy was performed using a Cary 300 instrument. Spectra were recorded in the diffuse reflectance mode using Spectralon® as white standard. Scans range was 240–800 nm.

XPS data were recorded on pellets using a customized system incorporating a hemispherical analyser (SPECS Phoibos 100), a non-monochromatized X-ray source (Al Kα; 1486.6 eV, Mg Kα, 1253.6 eV). The analyser was operated at a fixed transmission and 50 eV pass energy with an energy step of 0.1 eV. Binding energies were calibrated using C *1 s* (284.6 eV) as an internal reference. Prior to each analysis, the samples were evacuated to 10^{-9} mbar at room temperature. In a typical experiment, the sample was initially placed in the sample holder and transferred to the spectrometer chamber where XPS spectra were acquired.

In-situ FTIR studies were performed in a Harricks praying mantis cell. The spectra were recorded on a Nicolet FT-IR spectrometer at reaction conditions with a resolution of 4 cm^{-1}. Before reaction, catalysts were pretreated in N_2 at 50 ºC for 30 min

Temperature programmed reduction (H_2-TPR) was performed using a Chemstar instrument (Quantachrome). About 30 mg of the catalysts previously degassed at 50 °C for 30 min under Ar flow. The TPR spectra were collected in 10 mL/min mixture of 5% H_2/Ar from 50 ºC to 700 °C with a heating rate of 10 °C/min.

Transmission electron microscopy were performed by using a FEI Tecnai F30 microscope in STEM mode operated at 300 kV equipped with a Gatan GIF Quantum 963 energy filter. The samples were directly dropped on a nickel grid.

2.2. Photocatalytic runs

Gas phase photocatalytic H_2 production tests were performed in a flow cell (Fig. 1). The powder photocatalysts (50 mg) were placed in the cell and then degassed with N_2 at 50 ºC. Methanol steam flow (CH_3OH = 20% v/v) at 15 mL/min was passed through the sample for 60 min before reaction. After which, the lamp (200 W lamp housing) was switched on and the sample was illuminated through the quartz top-window of the cell. Effluent gases were analysed to quantify H_2 production by gas chromatography (Agilent microGC) using a thermal conductivity detector. Only CO and CO_2 were detected as side products. CO selectivity (S_{CO}) were calculated by considering all products detected:

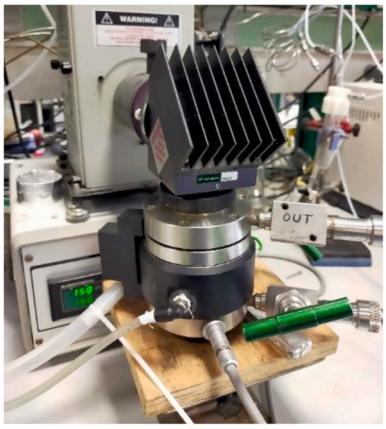

Fig. 1. Photocatalytic gas-phase flow-reactor used for thermo-photocatalytic runs.

$$S_{CO}(\%) = \frac{[CO]}{([H_2] + [CO] + [CO_2])} \times 100$$

Thermo-photocatalytic runs were performed at 200 ºC. As we have evidenced in a previous study, at this temperature the synergistic effect for thermo-photocatalytic process is maximum [29]. As reference, thermo-catalytic runs were performed in the absence of light under similar reaction conditions.

The apparent quantum efficiency for the H_2 evolution reaction has been determined from the reaction rate and the flux of incoming photons (calculated for the irradiation wavelengths of 365 nm) [20,30].

$$AQE = \frac{rate \quad (mol{\cdot}s^{-1})}{rate \quad of \quad incident \quad photons \quad (mol{\cdot}s^{-1})}$$

The synergetic effect of the thermal contribution on thermo-photocatalytic process was evaluated by considering the difference rate with single process rates [31].

$$rate_{syn} = rate_{thermo-photo} - \left(rate_{photo} + rate_{thermo}\right)$$

From this $rate_{syn}$ value we have calculated the synergetic efficiency (AQE_{syn}) which specifically accounts the efficiency attributable to the synergy of both thermo- and photo-catalytic processes.

3. Results and discussions

3.1. Copper features study with metal content

Copper deposition over TiO_2 by chemical reduction leads to well dispersed Cu nanoparticles over the range of studied systems. As it can be observed from STEM images (Fig. 2), homogeneous dispersion of Cu nanoparticles of ca. 2 nm is obtained. Moreover, no aggregation of Cu clusters is noticed as metal loading increases.

From diffuse reflectance spectra (Fig. 3), important absorption bands can be found at 350–450 nm and 750 nm that can be attributed to Cu clusters at the surface. These new bands progressively increase as copper loading increases, specially bands at 410 nm and 750 nm. Thus, bands within the range 350–450 nm have been ascribed to $(Cu–O–Cu)^{2+}$

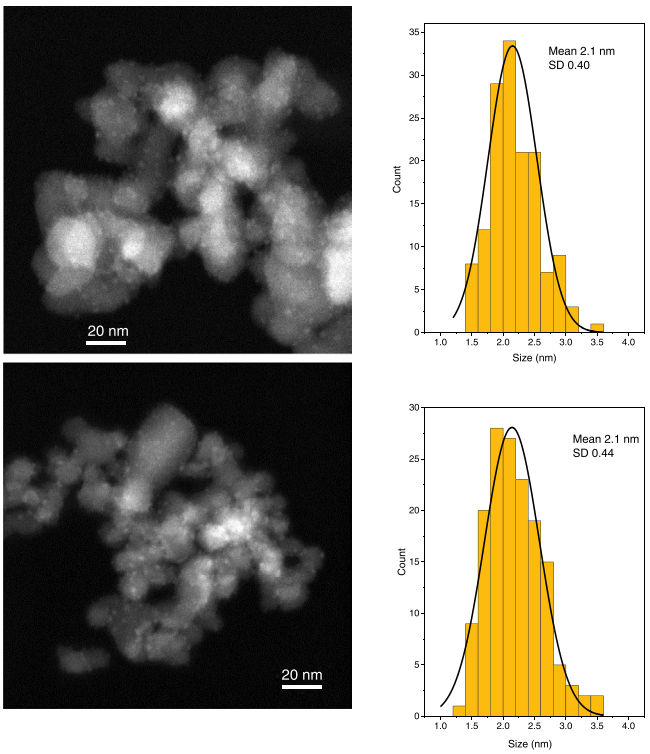

Fig. 2. HAADF images for Cu3P90 (*upper panel*) and Cu5P90 (*lower panel*) systems.

clusters in a highly dispersed state as well as to three-dimensional Cu^{1+} clusters. [32,33] On the other hand, the band at 750–850 nm has been assigned to $^2E_g \rightarrow {}^2T_{2\,g}$ transitions of Cu^{2+} located in the distorted or perfect octahedral symmetry. [34] From these results, we could expect that Cu species would consist on highly dispersed CuO and surface doped $Cu^{2+/1+}$. Both bands progress similarly as metal content increases (Fig. 3.b).

Reduction profile also denotes the evolution of copper clusters as loading increases (Fig. 4). In all cases a single TPR peak ca. 180 ºC is found for all catalysts. This is a rather lower reduction temperature compared with values reported in the literature, and would be attributed to highly dispersed CuO species at the nanoscale. [35–37] Moreover, from the deconvolution of TPR peaks it is possible to envisage four Cu species, denoted as α to δ. The presence of different reduction peaks in the TPR profile of oxide-supported Cu samples has been extensively reported. [38,39] Thus, it is accepted that large and crystallized CuO particles would be reduced at higher temperature than smaller CuO clusters or highly dispersed Cu^{2+} species in strong interaction with the oxide support. [40,41] In our case, the reduction temperature around 180 ºC clearly points out the absence of bulk CuO, as was stated above from TEM images. For all samples, species reduced at slightly higher temperature ($\gamma + \delta$) are prominent. However, as metal loading increases, low reduction temperature species ($\alpha + \beta$) become more evident (Fig. 4.**b**). Such low reduction temperature species would be associated to finely disperse copper species as support Cu^{2+} doped and would be hardly detected from TEM analysis. So, only small CuO nanoclusters are noticed. Therefore, for higher Cu content catalyst, Cu species distribution seems to be composed equally by small finely disperse CuO nanoclusters and surface doped Cu^{2+} species. Quantitative analysis from H_2 consumption clearly denotes the efficiency of deposition method. The amount of reduced Cu follows a clear linear evolution being in all cases close to the nominal values (Fig. 4.c).

From XPS analysis, the observed broad peaks as well as the presence of a shake-up satellite would denote the coexistence of Cu^{2+} and Cu^{+}/Cu species (Fig. 5.**a**). Thus, peaks at 932.0 eV and 951.9 eV would correspond to Cu $2p_{3/2}$ and Cu $2p_{1/2}$ spin-orbit split of Cu/Cu_2O species. [42] On the other hand, a second contribution at 934.2 eV and 954.1 eV with satellite shakeup at ca. 942 eV, in all the synthesized products should correspond to CuO species. It is also worthy to mention that for lower Cu contents, partially reduced fraction seems to be slightly higher (Table 1). This fact could be explaining considering a higher dispersion in these samples. Such low dimensional CuO clusters should be easily reduced under XPS conditions.

In agreement with TPR analysis, the surface Cu/Ti ratios calculated from XPS signals also follows a linear progression with nominal values, indicating the homogeneous distribution of Cu species over TiO_2 surface even at large metal loadings (Fig. 5.b). The Cu/Ti ratios obtained for samples after thermo-catalytic or thermo-photocatalytic runs at 200 ºC do not show a significant variation from fresh sample (Table 1). Therefore, no aggregation should be expected after reaction by effect of temperature.

Moreover, as Cu content increases the ratio of oxidized Cu seems to be slightly increased (Table 1), similarly as $\alpha + \beta$ family evolution from TPR experiment. This can be also observed from satellite relative intensity ($I_{sat}/I_{Cu2p3/2}$), showing the highest value for Cu4P90 catalyst. Indeed, $\alpha + \beta$ family has been previously associated to small CuO nanoclusters. The higher partial reduced fraction in low Cu content catalysts could therefore be ascribed to highly disperse Cu^{2+} entities ($\gamma + \delta$ species) that would easily reduce under XPS conditions.

3.2. *Thermo-photocatalytic performance of Cu/TiO_2 system*

Fig. 6 shows the H_2 production rates and apparent efficiencies and H_2

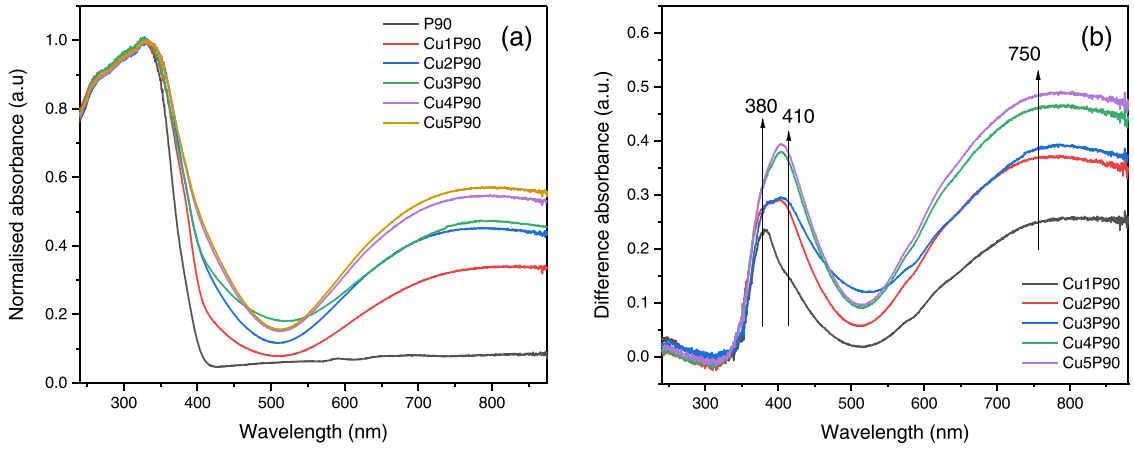

Fig. 3. a) DRS spectra for Cu/TiO_2 systems; b) Difference spectra of different Cu/TiO_2 samples with respect to bare TiO_2.

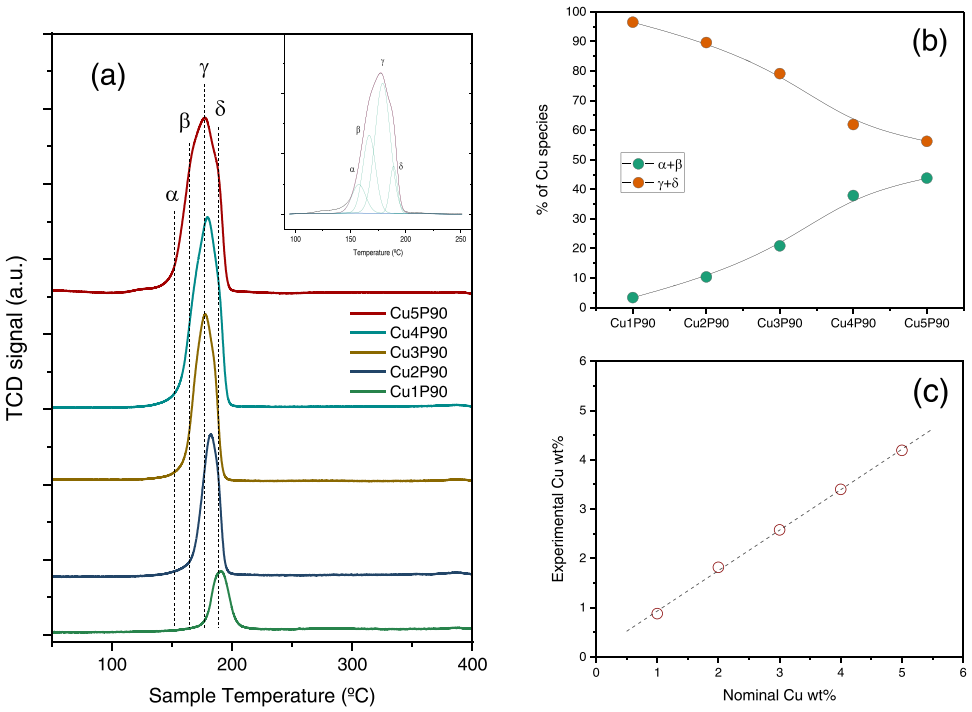

Fig. 4. a) H_2-TPR profiles (inset shows the deconvolution analysis for Cu5P90 TPR), b) evolution of different Cu species with content; and c) calculated Cu content from H_2 consumption for Cu/TiO_2 systems.

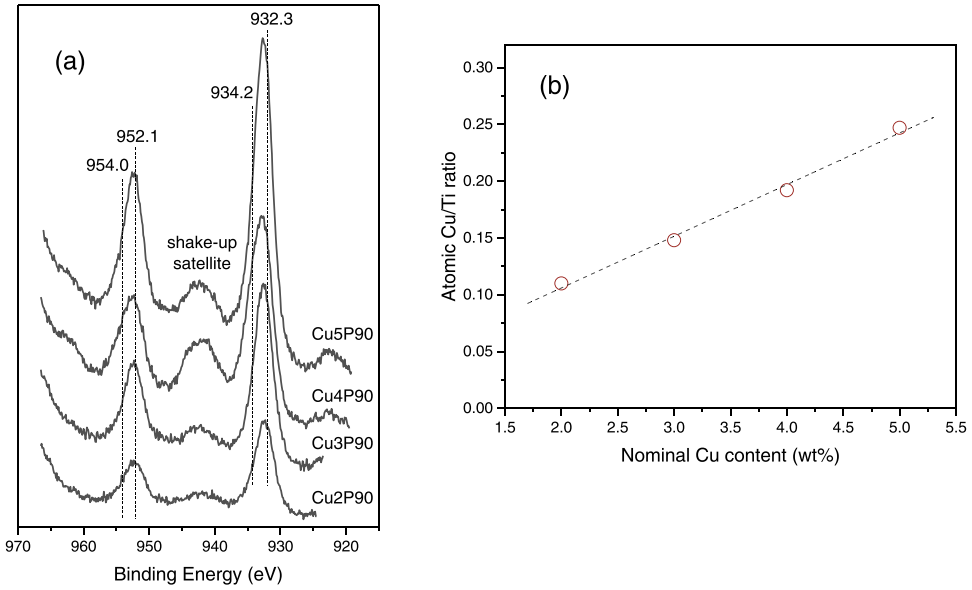

Fig. 5. a) XPS Cu *2p* spectra and b) surface Cu/Ti ratios for Cu/TiO_2 systems from XPS analysis.

Table 1
XPS analysis for Cu/TiO_2 systems.

	Surface at%		$I_{sat}/I_{Cu2p_{3/2}}$	Cu/Ti ratio
	Cu^{+}/Cu^{0}	Cu^{2+}		
Cu2P90	81	19	0.12	0.110
T200	70	30		0.109
TP200	77	23		0.114
Cu3P90	82	18	0.12	0.148
Cu4P90	59	41	0.25	0.192
Cu5P90	65	35	0.19	0.247

yields of Cu/TiO_2 P90 systems. Thus, the obtained rates for photo-, thermo-, and thermo-photocatalytic runs under UV–vis light illumination for 4 h are summarized in Table 2. As it can be observed, the performance for thermo-photocatalytic H_2 production are notably higher in all cases with respect to single thermo- and photocatalytic processes (Fig. S1).

The apparent quantum efficiencies denote that for photocatalytic performance the maximum value is attained for Cu2P90 catalyst, showing an H_2 production of 12 mmol/h·g after 4 h (Fig. 6.a). A higher Cu loading negatively affects to the photoreforming activity. In principle, the higher photoactivity exhibited by Cu2P90 would be associated to the finely dispersion and stronger interaction with support observed

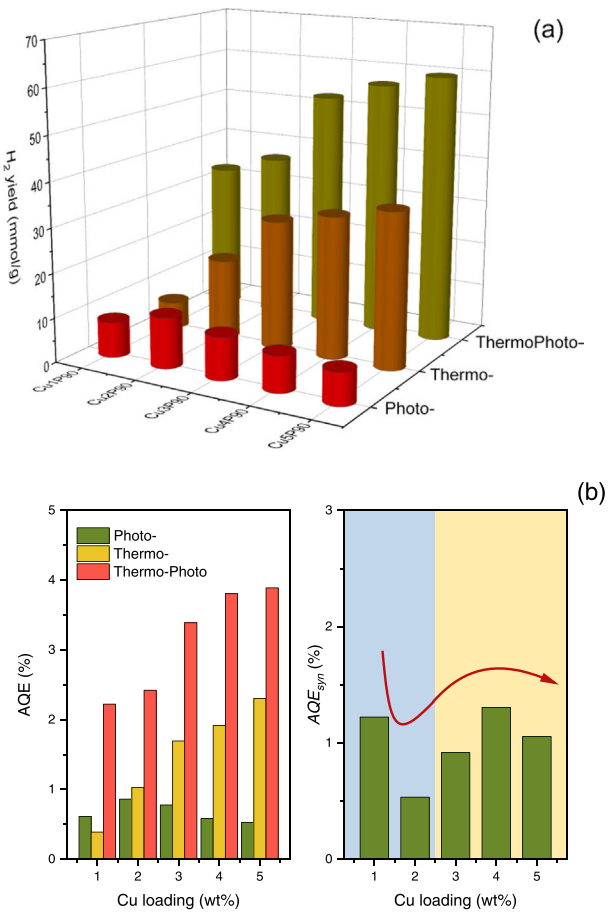

Fig. 6. a) H_2 production and b) Photonic Efficiencies (*AQE* and AQE_{syn}) for Cu/TiO_2 systems after 4 h of reaction.

Table 2
Rates for the H_2 photoreforming under different conditions.

Catalysts	Reforming rate (mmol/h·g) @ 4 h		
	50 °C	T 200°C	TP 200°C
Cu1P90	2.2	1.4	8.0
Cu2P90	3.1	3.7	8.7
Cu3P90	2.8	6.1	12.2
Cu4P90	2.1	6.9	14.0
Cu5P90	1.9	8.3	14.0

from TPR. [43] As metal loading increases, recombination processes would hinder the photocatalytic performance.

It can be also stated that thermo-catalytic process also leads to significant production of H_2. As we already discussed, H_2 formation under these conditions could be explained considering methanol thermal decomposition (Eq. i) [44,45].

$$CH_3OH \rightarrow 2\,H_2 + CO \quad methanol\ decomposition \qquad \text{Eq. i}$$

In this case, *AQE* values lineally increases in the whole range of Cu content, reaching an H_2 yield of ca 30 mmol/h·g for Cu5P90 catalyst (Fig. 6.a). Therefore, in this case and within the range of metal content studied, thermo-catalytic activity is clearly favoured by the increasing surface Cu over TiO_2.

Finally, the combined thermo-photoreforming leads to notable values of efficiency, with a maximum yield of ca. 60 mmol/h·g also for Cu5P90 catalyst. However, in this case the photocatalytic performance of Cu5P90 is close to that exhibited by Cu4P90 denoting certain exhausting effect in the thermo-photocatalytic activity with increasing metal loading. Thus, at this Cu loading the optimum metal content could be considered. (Fig. 6.a).

Since calculated $rate_{syn}$ always show positive values, the combined process cannot be explained as the sum of both single ones, and a certain synergistic effect can be envisaged for all catalysts. Moreover, the calculated AQE_{syn} clearly denote that the combination of thermo- and photo- processes notably affects to the overall reaction performance and appear clearly affected by metal loading (Fig. 6.b).

In this sense, it is also interesting to highlight the evolution of the synergy with Cu loading (Fig. 6.b). For the lowest Cu content, since the photocatalytic performance is rather low, thermal contribution appears important. Minimum AQE_{syn} is found for Cu2P90, for which the photocatalytic performance is maximum. Thermal-photocatalytic synergy reaches a minimum for Cu2P90 catalyst, for which photocatalytic performance is maximum and thermo-catalytic activity is still low. Catalysts with metal contents higher than 2 showed outstanding thermo-photocatalytic *AQE* that progressively increases with Cu content. However, though thermal reforming lineally grows with Cu, a maximum in the AQE_{syn} is found for Cu4P90 catalysts. This fact would point out a process that would hinder the thermo-photocatalytic performance for Cu5P90.

In order to understand the evolution showed by *AQE* and AQE_{syn} in different studied photoreforming processes, we followed CO and CO_2 as interesting intermediates from side reactions that would simultaneously take place (Fig. 7). Thus, CO can be derived from side reactions that would proceed simultaneously with photoreforming; that is, methanol decomposition as well as formic acid dehydration (Eqs. i and ii) [45].

$$HCOOH \rightarrow H_2O + CO \quad formic\ \ acid\ \ dehydration \qquad \text{Eq. ii}$$

From the evolution of CO selectivity, the single photocatalytic process clearly denotes a concomitant formation of CO. The observed CO formation progressively decreases as Cu loading increases. For the thermocatalytic process, low amounts of copper do not lead to CO formation, starting at Cu loading higher than 2 wt%. It is worthy to notice that the combine thermo-photocatalytic process shows a similar trend as photocatalytic one, but with much lower CO selectivity. Thus, for higher Cu loading S_{CO} values are similar to that obtained by thermocatalysis.

The marked lower S_{CO} values attained for thermo- and thermo-photocatalytic processes would denote an important CO consumption (probably associated with a higher H_2 yield).

Thus, two probable processes could be involved to explain the lower CO formation and higher H_2 production. On one hand, formic acid

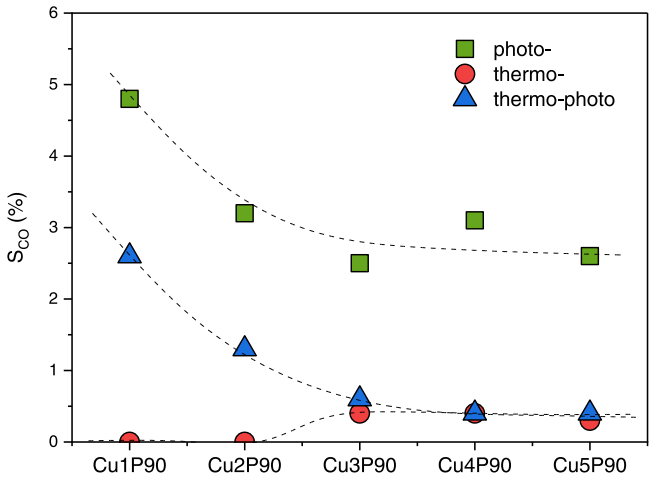

Fig. 7. CO Selectivity during the gas-phase methanol thermo-photocatalytic reforming using Cu/TiO_2 after 4 h of reaction.

dehydrogenation as alternative way to decompose formic acid instead of dehydration; and water gas shift reactions (Eqs. iii and iv). Indeed, the occurrence of water-gas-shift reaction has been previously argued within H_2 photoreforming reaction [29,44].

$$HCOOH \rightarrow H_2 + CO_2 \; dehydrogenation \qquad \text{Eq. iii}$$

$$CO + H_2O \rightarrow H_2 + CO_2 \; water\ gas\ shift\ (WGS) \qquad \text{Eq. iv}$$

We may also point out that the presence of CO during photoreforming reaction would probably affect to the photocatalytic activity during the reaction time by CO poisoning of the metal active sites [46,47].

3.3. *In-situ FTIR analysis of thermo-photocatalytic reaction*

In Fig. 8 we depict the FTIR spectra during in-situ photoreforming reaction. From these spectra, two important regions can be envisaged. In the higher wavenumber region, C–H stretching modes can be found. Thus, C–H contributions at 2920/2820 cm^{-1} have been associated to metoxy species [45,48]. The appearance of these bands is accompanied by a negative broad peak at around 3620 cm^{-1} due to the disappearance of surface hydroxyl groups through the dissociative adsorption of methanol. As described in the literature, the C–O stretching region located in the region 1800–700 cm^{-1} also shows the characteristics bands associated to methanol. Thus, at room temperature it can be notice a sharp band at around 1060 and 1135 cm^{-1} that can be ascribed to C–O stretching modes of methoxy group. The evolution of bands in this region during different experimental conditions is similar for all catalysts, varying the relative intensity of certain bands. Thus, during photocatalytic experiment at 50 ºC, new intense bands appear within this region at 1580 cm^{-1} and 1360 cm^{-1}. These new bands can be ascribed respectively to the υ_{as}(COO) and υ_s(COO) for bidentate formate ions adsorbed on TiO_2 surface. The intensity of these bands remains almost similar as Cu loading increases for Cu contents higher than 2 wt% (Fig. S2). It is worthy to mention that these bands do not appear during thermal treatment. In this case, only the band at 1135 cm^{-1} seems to be exalted (Fig. S2).

Concerning the thermo-photocatalytic process, as temperature increases, bands associated to formates become notably marked. However, at 200 ºC these bands completely disappear. At 120 ºC, such bands are noticeable, showing exponential growing intensities as Cu content increases (Fig. S2). Therefore, the formation of formates seems to be clearly favoured by the increasing metal sites. As previously stated, the presence of formates would determine the different evolution of CO.[29] Thus, for photocatalytic runs we have already showed that S_{CO} values were particularly lower with respect to those found for thermo- and thermo-photocatalytic experiments (Fig. 8). These two facts can be correlated by considering formic acid dehydration reaction which leads to the formation of CO and H_2O. As above discussed, during thermo-photocatalytic experiment, at moderate temperatures the formation of formates was exalted and increases with Cu content. It is clear that formate formation is favoured by temperature.

The absence of formate bands at reaction temperature clearly indicates that they were completely transformed into CO through dehydration. At the same time, we have also stated that S_{CO} drastically decays. Therefore, during thermo-catalytic reforming at 200 ºC the outstanding H_2 formation can be ascribable to the enhanced transformation of methanol into formate which proceed to CO and then through WGS reaction to H_2 formation. From both facts it would be inferred that WGS reaction is playing an important role. In this sense, the higher the Cu load, the more important the WGS reaction becomes in the overall process.

Thus, it can be argued that the efficiency of the thermo-photocatalytic reaction over Cu/TiO_2 systems would be improved with Cu loading. Thus, the different optimum Cu loading attained for photocatalytic and thermo-photocatalytic reforming was conditioned by the thermal contribution through WGS reaction. From these results, it seems that this later process would be favoured by increasing Cu loadings. Thus, while for photocatalytic reforming Cu2P90 showed the optimum value, for the combined thermo-photocatalytic process Cu5P90 would be the best catalyst.

Therefore, we evidenced a clear dependency of the mechanism on the metal content. Moreover, as we stated from TPR and XPS Cu species present in each case is different. Thus, while for Cu2P90 Cu^{2+} with strong interaction with support are the predominant, for Cu5P90 CuO dispersed nanoclusters would be also present. The influence of cluster size on the photocatalytic performance of H_2 photoreforming was studied by Zheng et al. which stated that small clusters usually possess higher charge separation efficiency [49]. In this sense, Li et al. showed that through ligand assisted method, ultrafine size clusters of Cu species (with about 1 nm), dispersed on the surface of TiO_2 were obtained [50]. These authors reported that the superior H_2 evolution performance of CuO/TiO_2 mainly originates from the cluster size and unique interfacial structure formed. On the other hand, CuO clusters modulated in the range 4–8 nm by controlling the loading amount of Cu and calcining temperature were obtained for photocatalytic WGS reaction [51]. Therefore, it is clear that different process would require not only a particular metal loading but also an optimum cluster size. Moreover, different copper species distribution could be also correlated with the better performance as temperature increases.

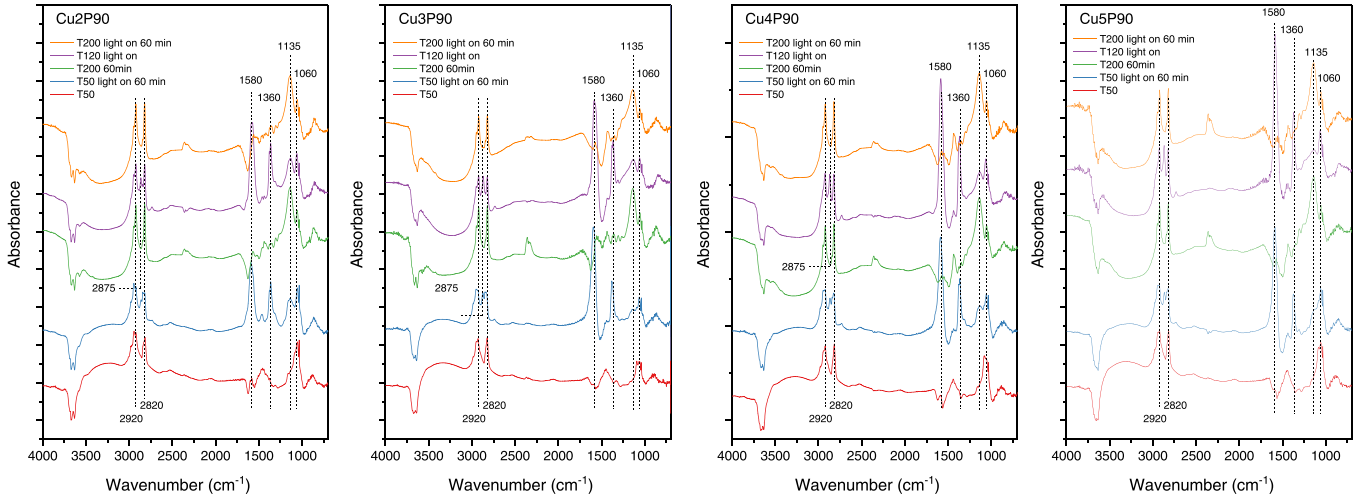

Fig. 8. *In situ* DRIFTS spectra of Cu/TiO_2 systems under methanol steam at different reaction conditions.

4. Conclusions

Copper supported TiO_2 with different metal loadings was used as catalyst for the gas phase methanol thermal photoreforming. From the wide characterization of the catalyst, we have shown that copper metal co-catalyst has been efficiently deposited and well dispersed on the support surface within the studied range of metal loading. We have stated the important synergistic effect in the thermal-photocatalytic reaction. Thus, ca 60 mmol/h·g_{cat} was obtained after 4 h at 200 ºC upon illumination. Different optimum metal loading can be envisaged for different methanol reforming experiments. Moreover, as increasing metal loading, the nature of Cu species seems to be modified, subsequently conditioning the catalytic performance. Thus, while for the photocatalytic reforming Cu2P90 was the best catalyst, the thermocatalytic reforming performance follows a lineal evolution with Cu content in the range of the studied metal content. For thermo-photocatalytic reforming, the optimum value would be Cu5P90 for which the synergistic improvement started to decay. During thermo-photocatalytic reaction different thermo- and photo-processes are involved, resulting in different optimal catalyst formulation. We have shown that while for photocatalytic reaction low co-catalyst loading leads to the better performance, for thermo-photocatalytic process higher loading is needed. These results clearly highlight the necessity of metal loading optimization due to the occurrence of different catalytic mechanism that simultaneously takes place during the thermo-photocatalytic reaction.

CRediT authorship contribution statement

F. Platero: Methodology, Investigation, Writing – original draft. **A. Caballero:** Conceptualization, Methodology, Supervision. **G. Colón:** Conceptualization, Methodology, Writing – original draft, Writing – review & editing, Supervision.

Declaration of Competing Interest

The authors declare that they have no known competing financial interests or personal relationships that could have appeared to influence the work reported in this paper.

Data Availability

Data will be made available on request.

Acknowledgments

Authors acknowledge the financial support from the EU FEDER and Junta de Andalucía under I+D+i Project P20-00156. We also acknowledge the financial support from PID2020-119946RB-I00 project funded by MCIN/AEI/ 10.13039/501100011033 and, as appropriate, by "ERDF A way of making Europe", by the "European Union".

Appendix A. Supporting information

Supplementary data associated with this article can be found in the online version at doi:10.1016/j.apcata.2022.118804.

References

[1] S. Wu, N. Salmon, M.M.J. Li, R. Bañares-Alcántara, S.C.E. Tsang, Energy decarbonization via green H_2 or NH_3? ACS Energy Lett. 7 (2022) 1021–1033.
[2] Q. Wang, K. Domen, Particulate photocatalysts for light-driven water splitting: mechanisms, challenges, and design strategies, Chem. Rev. 120 (2020) 919–985.
[3] W.H. Chen, J.E. Lee, S.H. Jang, S.S. Lam, G.H. Rhee, K.J. Jeon, M. Hussain, Y. K. Park, A review on the visible light active modified photocatalysts for water splitting for hydrogen production, Int. J. Energy Res. 46 (2022) 5467–5477.
[4] C. Konstantinos, P. Fornasiero, Photocatalytic hydrogen production: a rift into the future energy supply, ChemCatChem 9 (2017) 1523–1544.
[5] N. Skillen, H. Daly, L. Lan, M. Aljohani, C.W.J. Murnaghan, X. Fan, C. Hardacre, G. N. Sheldrake, P.K.J. Robertson, Photocatalytic reforming of biomass: what role will the technology play in future energy systems, Top. Curr. Chem. 380 (2022) 33.
[6] L. Clarizia, G. Vitiello, G. Luciani, I. Somma, R. Andreozzi, R. Marotta, Hydrogen generation through solar photocatalytic processes: a review of the configuration and the properties of effective metal-based semiconductor nanomaterials, Appl. Catal. A: Gen. 518 (2016) 142–149.
[7] D.S.M. Constantino, M.M. Dias, A.M.T. Silva, J.L. Faria, C.G. Silva, Intensification strategies for improving the performance of photocatalytic processes: a review, J. Clean. Prod. 34015 (2022), 130800.
[8] M.I. Maldonado, A. López-Martín, G. Colón, J. Peral, J.I. Martínez-Costa, S. Malato, Solar pilot plant scale hydrogen generation by irradiation of Cu/TiO_2 composites in presence of sacrificial electron donors, Appl. Catal. B Environ. 229 (2018) 15–23.
[9] S.Y. Toledo-Camacho, A. Rey, M.I. Maldonado, J. Llorca, S. Contreras, F. Medina, Photocatalytic hydrogen production from water-methanol and -glycerol mixtures using Pd/TiO_2(-WO_3) catalysts and validation in a solar pilot plant, Int. J. Hydrog. Energy 46 (2021) 36152–36166.
[10] H. Nishiyama, T. Yamada, M. Nakabayashi, Y. Maehara, M. Yamaguchi, Y. Kuromiya, Y. Nagatsuma, H. Tokudome, S. Akiyama, T. Watanabe, R. Narushima, S. Okunaka, N. Shibata, T. Takata, T. Hisatomi, K. Domen, Photocatalytic solar hydrogen production from water on a 100-m^2 scale, Nature 598 (2021) 304–307.
[11] A. Ruiz-Aguirre, J.G. Villachica-Llamosas, M.I. Polo, A. Cabrera-Reina, G. Colón, J. Peral, S. Malato, Assessment of Solar Photocatalytic Hydrogen Generation through Pilot Plant Scale Multiple Approaches: Valorisation, Water Decontamination and Disinfection. Energy (submitted).
[12] A. Kubacka, M. Fernández-García, G. Colón, Advanced nanoarchitectures for solar photocatalytic applications, Chem. Rev. 112 (2012) 1555–1614.
[13] K.C. Christoforidis, P. Fornasiero, Photocatalysis for hydrogen production and CO_2 reduction: the case of copper-catalysts, ChemCatChem 2019 (2019) 368–382.
[14] G. Colón, Towards the hydrogen production by photocatalysis, Appl. Catal. A Gen. 518 (2016) 48–59.
[15] H. Wang, L. Zhang, Z. Chen, J. Hu, S. Li, Z. Wang, J. Liu, X. Wang, Semiconductor heterojunction photocatalysts: design, construction, and photocatalytic performances, Chem. Soc. Rev. 43 (2014) 5234–52447.
[16] M. Serra, J. Albero, H. García, Photocatalytic activity of Au/TiO_2 photocatalysts for H_2 evolution: role of the Au nanoparticles as a function of the irradiation wavelength, ChemPhysChem 16 (2015) 1842–1845.
[17] Z.H.N. Al-Azri, M. Aloufi, A. Chan, G.I.N. Waterhouse, H. Idriss, Metal particle size effects on the photocatalytic hydrogen ion reduction, ACS Catal. 9 (2019) 3946–3958.
[18] F. Platero, A. López-Martín, A. Caballero, T.C. Rojas, M. Nolan, G. Colón, Overcoming Pd−TiO_2 deactivation during H_2 production from photoreforming using Cu@Pd nanoparticles supported on TiO_2, ACS Appl. Nano Mater. 4 (2021) 3204–3219.
[19] B. Mei, K. Han, G. Mul, Driving surface redox reactions in heterogeneous photocatalysis: the active state of illuminated semiconductor-supported nanoparticles during overall water-splitting, ACS Catal. 8 (2018) 9154–9164.
[20] J.M. Valero, S. Obregón, G. Colón, Active site considerations on the photocatalytic H_2 evolution performance of Cu-doped TiO_2 obtained by different doping methods, ACS Catal. 4 (2014) 3320–3329.
[21] V. Kumaravel, S. Mathew, J. Bartlett, S.C. Pillai, Photocatalytic hydrogen production using metal doped TiO_2: a review of recent advances, Appl. Catal. B: Environ. 5 (2019) 1021–1064.
[22] J.S. Schubert, L. Kalantari, A. Lechner, A. Giesriegl, S.P. Nandan, P. Alaya, S. Kashiwaya, M. Sauer, A. Foelske, J. Rosen, P. Blaha, A. Cherevan, D. Eder, Elucidating the formation and active state of Cu co-catalysts for photocatalytic hydrogen evolution, J. Mater. Chem. A 9 (2021) 21958–21971.
[23] M. Haddad, A. Belhadi, L. Boudjellal, M. Trari, Photocatalytic hydrogen production on the heterojunction CuO/ZnO, Int. J. Hydrog. Energy 46 (2021) 37556–37563.
[24] A. Caravaca, H. Daly, M. Smith, A. Mills, S. Chansai, C. Hardacre, Continuous flow gas phase photoreforming of methanol at elevated reaction temperatures sensitised by Pt/TiO_2, React. Chem. Eng. 1 (2016) 649–657.
[25] U. Caudillo-Flores, G. Agostini, C. Marini, A. Kubacka, M. Fernández-García, Hydrogen thermo-photo production using Ru/TiO_2: heat and light synergistic effects, Appl. Catal. B: Environ. 256 (2019), 117790.
[26] V. Nair, M.J. Muñoz-Batista, M. Fernández-García, R. Luque, J.C. Colmenares, Thermo-photocatalysis: environmental and energy applications, ChemSusChem 12 (2019) 2098–2116.
[27] I. Barba-Nieto, N. Gómez-Cerezo, A. Kubacka, M. Fernández-García, Oxide-based composites: applications in thermo-photocatalysis, Catal. Sci. Technol. 11 (2021) 6904–6930.
[28] Z. Wang, Z. Yang, Z. Yang, R. Fang, Y. Yan, J. Ran, L. Zhang, A. State-of-the-art, review on action mechanism of photothermal catalytic reduction of CO_2 in full solar spectrum. Chem. Engineer, J 4291 (2022), 132322.
[29] A. López-Martín, F. Platero, A. Caballero, G. Colón, Thermo-photocatalytic methanol reforming for hydrogen production over a CuPd–TiO_2 catalyst, ChemPhotoChem 4 (2020) 1–9.
[30] M. Qureshi, K. Takanabe, Insights on measuring and reporting heterogeneous photocatalysis: efficiency definitions and setup examples, Chem. Mater. 29 (2017) 158–167.
[31] U. Caudillo-Flores, M.J. Muñoz-Batista, M. Fernández-García, A. Kubacka, Bimetallic Pt-Pd co-catalyst Nb-doped TiO_2 materials for H_2 photo-production under UV and visible light illumination, Appl. Catal. B Environ. 238 (2018) 533–545.

[32] G. Colón, M. Maicu, M.C. Hidalgo, J.A. Navío, Cu-doped TiO_2 systems with improved photocatalytic activity, Appl. Catal. B Environ. 67 (2006) 41–51.
[33] V. Polliotto, S. Livraghi, A. Krukowska, M.V. Dozzi, A. Zaleska-Medynska, E. Selli, E. Giamello, Copper-modified TiO_2 and $ZrTiO_4$: Cu oxidation state evolution during photocatalytic hydrogen production, ACS Appl. Mater. Interfaces 10 (2018) 27745–27756.
[34] B. Li, Y. Hao, B. Zhang, X. Shao, L. Hu, A multifunctional noble-metal-free catalyst of CuO/TiO_2 hybrid nanofibers, Appl. Catal. A Gen. 531 (2017) 1–12.
[35] M.K. Kumar, K. Bhavani, G. Naresh, B. Srinivas, A. Venugopal, Plasmonic resonance nature of Ag-Cu/TiO_2 photocatalyst under solar and artificial light: Synthesis, characterization and evaluation of H_2O splitting activity, Appl. Catal. B Environ. 199 (2016) 282–291.
[36] Q. Shi, G. Ping, X. Wang, H. Xu, J. Li, J. Cui, H. Abroshan, H. Ding, G. Li, CuO/TiO_2 heterojunction composites: an efficient photocatalyst for selective oxidation of methanol to methyl formate, J. Mater. Chem. A 7 (2019) 2253–2260.
[37] M.K. Kumar, G. Naresh, V.V. Kumar, B.S. Vasista, B. Sasikumar, A. Venugopal, Improved H_2 yields over Cu-Ni-TiO_2 under solar light irradiation: behaviour of alloy nano particles on photocatalytic H_2O splitting, Appl. Catal. B Environ. 299 (2021), 120654.
[38] M. Hinojosa-Reyes, R. Camposeco-Solís, R. Zanella, V. Rodríguez González, Hydrogen production by tailoring the brookite and Cu_2O ratio of sol-gel Cu-TiO_2 photocatalysts, Chemosphere 184 (2017) 992–1002.
[39] G. Cao, N.A. Deskins, N. Yi, Carbon monoxide oxidation over copper and nitrogen modified titanium dioxide, Appl. Catal. B Environ. 285 (2021), 119748.
[40] H. Xue, T. Meng, F. Liu, X. Guo, S. Wang, D. Mao, Enhanced resistance to calcium poisoning on Zr-modified Cu/ZSM-5 catalysts for the selective catalytic reduction of NO with NH_3, RSC Adv. 9 (2019) 38477–38485.
[41] C. Li, Y. Yang, W. Ren, J. Wang, T. Zhu, W. Xu, Effect of Ce Doping on Catalytic Performance of Cu/TiO_2 for CO Oxidation, Catal. Lett. 150 (2020) 2045–2055.
[42] M.E. Aguirre, R. Zhou, A.J. Eugene, M.I. Guzman, M.A. Grela, Cu_2O/TiO_2 heterostructures for CO_2 reduction through a direct Z-scheme: protecting Cu_2O from photocorrosion, Appl. Catal. B: Environ. 217 (2017) 485–493.
[43] Y. Qi, Z. Yang, Y. Jiang, H. Han, T. Wu, L. Wu, J. Liu, Z. Wang, F. Wang, Platinum−copper bimetallic nanoparticles supported on TiO_2 as catalysts for photo−thermal catalytic toluene combustion, ACS Appl. Nano Mater. 5 (2022) 1845–1854.
[44] S. Fang, Z. Sun, Y.H. Hu, Insights into the thermo-photo catalytic production of hydrogen from water on a low-cost NiOx-loaded TiO_2 catalyst, ACS Catal. 9 (2019) 5047–50567.
[45] F. Platero, A. López-Martín, A. Caballero, G. Colón, Mechanistic considerations on the H_2 production by methanol thermal-assisted photocatalytic reforming over Cu/TiO_2 catalyst, ChemCatChem 13 (2021) 1–12.
[46] Y.J. Zhang, V. Sethuraman, R. Michalsky, A.A. Peterson, Competition between CO_2 reduction and H_2 evolution on transition metal electrocatalysts, ACS Catal. 4 (2014) 3742–3748.
[47] W. Chen, J. Cao, W. Fu, J. Zhang, G. Qian, J. Yang, D. Chen, X. Zhou, W. Yuan, X. Duan, Molecular-level insights into the notorious CO poisoning of platinum catalyst, Angew. Chem. Int. Ed. 61 (2022), e202200190.
[48] U. Caudillo-Flores, I. Barba-Nieto, M.J. Muñoz-Batista, D. Motta-Meira, M. Fernández-García, A. Kubacka, Thermo-photo production of hydrogen using ternary Pt-CeO_2-TiO_2 catalysts: a spectroscopic and mechanistic study, Chem. Eng. J. 425 (2021), 130641.
[49] C. Zheng, H. Bu, F. Yang, Z. Xu, H. Zhao, Size effect of (CuO) n ($n = 1 \backsim 6$) clusters on the modification of rutile-TiO_2 photocatalysts, Energy Technol. (2021), 2100161.
[50] Y.H. Li, L.R. Zeng, H.G. Yang, A novel strategy for tailoring copper oxide cluster with Pt-like activity for photocatalytic hydrogen evolution, Int. J. Hydrog. Energy 40 (2015) 15454–15459.
[51] L. Zhao, Y. Qi, L. Song, S. Ning, S. Ouyang, H. Xu, J. Ye, Solar-driven water–gas shift reaction over CuO_x/Al_2O_3 with 1.1% of light-to-energy storage, Angew. Chem. Int. Ed. 58 (2019) 7708–7712.